

# Probing High-Order Transient Oligomers using Ion Mobility Mass Spectrometry coupled to Infrared Action Spectroscopy

Sjors Bakels<sup>1,2</sup>, Steven Daly<sup>3</sup>, Berk Doğan<sup>3</sup>, Melissa Baerenfaenger<sup>1,2</sup>, Jan Commandeur<sup>3</sup>, and Anouk M. Rijs<sup>1,2\*</sup>

<sup>1</sup> Division of Bioanalytical Chemistry, Department of Chemistry and Pharmaceutical Sciences, Amsterdam Institute of Molecular and Life Sciences, Vrije Universiteit Amsterdam, De Boelelaan 1105, 1081 HV Amsterdam, The Netherlands.

<sup>2</sup> Centre for Analytical Sciences Amsterdam, 1098 XH, Amsterdam, The Netherlands.

<sup>3</sup> MS Vision, Spectrometry Vision B.V., Televisieweg 40, Almere 1322 AM, The Netherlands

---

**ABSTRACT:** Understanding and controlling peptide aggregation is critical due to its neurotoxic implications. However, structural information on the key intermediates, the oligomers, is obscured by a cascade of coinciding events occurring at various time and energy scales, which results in complex and heterogeneous mixtures of oligomers. To address this challenge, we have developed the Photo-Synapt, a novel, multidimensional spectrometer that integrates ion mobility mass spectrometry with infrared (IR) action spectroscopy within a single experiment. By combining three different, orthogonal analytical dimensions, we can select and isolate individual oligomers by mass, charge, size and shape and provide a unique molecular fingerprint for each oligomer. The broad application of this technology is demonstrated by its application to oligosaccharide analysis from glycoproteins, which are challenging to analyze due to the minute differences between isomers. By integrating infrared action spectroscopy with ion mobility mass spectrometry, this approach adds an analytical dimension that effectively addresses this limitation, offering a unique molecular fingerprint for each isomer.

---

Nature has many examples where not only function, but also malfunction arises from complex processes. An important example of such a highly complex molecular mechanism is that of aggregating peptides and proteins. Aggregation, the transition from soluble functioning proteins into insoluble amyloid aggregates, is directly related to several human neurodegenerative diseases including Alzheimer's and Parkinson's disease.<sup>1-7</sup> In these aggregation processes, complexity arises from the diversity of intermediate, soluble oligomeric species and the numerous possible reaction pathways that connect them. Our understanding of the early stages of protein aggregation is hampered by the heterogeneity that results. This is particularly important as neurotoxicity originates from the soluble, oligomeric intermediates that are formed early on the aggregation pathway.<sup>2, 3</sup> Understanding this complexity and unraveling the early steps of the molecular aggregation network is key to regulate and ideally stop these phenomena. This requires an experimental approach that can selectively pick one specific intermediate from the heterogeneous ensemble at specific points in time and to unravel its structure.

Ion Mobility Mass Spectrometry (IM-MS) has proven to be a powerful approach in elucidating the structural information of specific ions within a heterogeneous mixture of low abundant analytes.<sup>8</sup> Here, the mobility of ions is measured, allowing the separation of these ions based on their size,

mass, shape, and charge. IM-MS has been employed in studying the aggregation process, probing the formation of early-stage aggregation intermediates.<sup>7, 9-19</sup>

Using IM-MS, oligomers of different sizes but with the same  $m/z$  value can be separated. In such experiments, mass spectrometry is used to select a specific set of oligomers with the same  $n^{z+}$  ( $[nM+zH]^{z+}$ ) where  $n$  is the number of monomer units in the oligomer and  $z$  is the number of charges. Subsequently, IM is used to separate individual oligomers with the same  $m/z$  ratio, and to identify each oligomer by their mobility and mobility selected mass spectra.<sup>18, 19</sup> Moreover, their overall structure can be deduced via their collision cross-sections (CCS).<sup>7, 20</sup> However, IM-MS is not sensitive to the secondary structure, and so cannot directly measure the expected increase in  $\beta$ -sheet character upon oligomer formation. To be able to directly measure such secondary structural changes, mass- and mobility-selected IR spectroscopy measurements are required. For example, Bowers, von Helden and Pagel *et al.* have combined infrared spectroscopy with IM-MS using a homebuilt set-up to probe the secondary structure of the segments NFGAIL from the unstructured human islet amyloid polypeptide (hIAPP, diabetes type II) and the peptide VEALYL from the insulin B chain. Using the C=O stretching vibrations (amide I band) between 1600 and 1800  $\text{cm}^{-1}$ , they could probe the onset of  $\beta$ -sheet formation.<sup>14, 21</sup>

This example is part of a growing trend of combining ion mobility mass spectrometry with either IR action spectroscopy and/or UV photodissociation (UVPD)<sup>22-25</sup>, either based on fully home-built instruments or modified commercial ion-mobility mass spectrometers, which has been reviewed in detail by Stroganova and Rijs.<sup>26</sup> Although the homebuilt systems have the benefit of being fully flexible, they lack the ease of use and support base of commercially available mass spectrometers. Moreover, these homebuilt spectrometers are typically integrated with free electron lasers at facilities and/or cryogenic-cooled IR spectroscopic methods.<sup>27, 28</sup> Focusing on the commercially based mass spectrometers, two types of hyphenated instruments exist: those starting with IR-MS where the ion mobility options are added later or ion mobility mass spectrometers where optical access is integrated. For the first option, either differential mobility spectrometry (DMS)<sup>29</sup> or field asymmetric ion mobility spectrometry (FAIMS)<sup>30</sup> has been placed at the front end of the mass spectrometer. Both DMS and FAIMS provide extra separation capabilities to the existing IR-MS workflow and are easy to implement. The high electric field nature of FAIMS, structural information via collision cross-section determination is not possible. In the recent years, modifying commercial MS instruments to add the spectroscopy capability has become more popular, by for example providing optical access and optical elements to direct the laser beam predominantly adding IR and/or UVPD to trapping mass spectrometers. Although only limited examples are shown for IM-MS with IR spectroscopy, UVPD (and XUV<sup>31</sup>) has been demonstrated previously on a Synapt<sup>22, 23</sup>, making it possible to probe isomeric species or conformational changes by UVPD after IM separation. These experiments could be performed in the trap or transfer TWave, where the pressures are  $\sim 5 \times 10^{-2}$  mbar and  $8 \times 10^{-3}$  mbar respectively. For IR spectroscopy, pressures of  $< 10^{-5}$  mbar are required with flexible irradiation times, demanding a different design.

Therefore, we have developed the Photo-Synapt, an ion mobility mass spectrometer (IM-MS) interfaced with infrared (IR) action spectroscopy in a single experiment. This was achieved by customizing a Synapt G2 mass spectrometer (Waters) to facilitate optical access, ion trapping and ion mobility slicing. An extra vacuum chamber was incorporated between the transfer TWave and the TOF region. This new chamber facilitates differential pumping to ensure the low pressures required for IR ion spectroscopy. Moreover, it contains two hexapoles and pin traps<sup>32, 33</sup>, which can be used to trap and manipulate ions over a long time. Optical access was arranged both orthogonally in the second pin trap, and parallel with the ion propagation direction. Tuneable IR light is provided using a small, turn-key table-top laser. Ion trapping and manipulation is performed using pulsed voltages controlled by a custom-made software. This includes modification of the existing ion optics to allow ion mobility slicing to be performed.

The Photo-Synapt spectrometer, all its modifications and mode of operations are described in detail in the following

section, while its wide scientific capabilities are demonstrated on selected experiments. Here, we will present the application of using the Photo-Synapt to study the early steps of peptide aggregation. Using mass-selection, a series of oligomers with the same  $m/z$  can be selected, and subsequently a single oligomer can be physically isolated via ion mobility slicing. We measure oligomer-specific vibrational spectra via IR action spectroscopy. Additionally, the broad impact of this three-dimensional IM-MS-IR combination has shown the structural identification of the sialic acid linkage isomers in glycans from glycoproteins. With the Photo-Synapt, it becomes possible to acquire unique mass and ion mobility-selected infrared spectra from mixtures of  $\alpha 2,6$ - and  $\alpha 2,3$ -linked sialic acid isomers, enabling their individual analysis and characterization.

Combining ion mobility, mass spectrometry, and IR spectroscopy in one experiment offers significant potential as a powerful analytical tool, allowing us to analyze the overall shape and size while obtaining detailed structural insights from vibrational spectroscopy. This hyphenated approach, integrating three orthogonal dimensions, facilitates the reduction of conformer heterogeneity and complexity, and enables the separation and structural identification of molecular isomers and oligomers.

## MODIFICATIONS OF THE SYNAPT

Figure 1 shows a schematic of the Photo-Synapt with its modifications to allow ion mobility slicing, ion trapping and UV/IR photofragmentation spectroscopy to be combined in a single experiment. The voltages presented in this section are for using the Photo-Synapt in positive mode.

**Source.** Unmodified electrospray (ESI) and nanospray (nESI) sources were used depending on the sample. To obtain better collisional cooling and hence improved transmission of high  $m/z$  species, the TWave ion guide was modified by inclusion of a pressure sleeve, which causes an increase in the pressure within the ion guide.<sup>32, 34</sup> In addition, a valve was added to the vacuum line of the source chamber which can be closed to further increase the pressure. The combined measures increase desolvation and transmission of large ions, and the modifications are presented in Figure S1 of the Supporting Information.

**Ion Mobility Slicing.** Ion mobility slicing is performed using the IMS Exit lens (indicated by B in Figure 1). In normal operation (both MS<sup>n</sup> and IM-MS) the lens is kept at a fixed voltage corresponding to maximum ion transmission. To perform mobility slicing, the lens is held at a lower potential to prevent ion transmission. The voltage is raised to allow transmission of ions of a given mobility, see Figure 2. The IMS start signal is used as a start trigger for a programmable delay ( $d$  in Figure 2) after which the lens is set high for a selected duration ( $w$  in Figure 2), allowing control over the mobility window to be transmitted (via control the delay of the sliced ions).

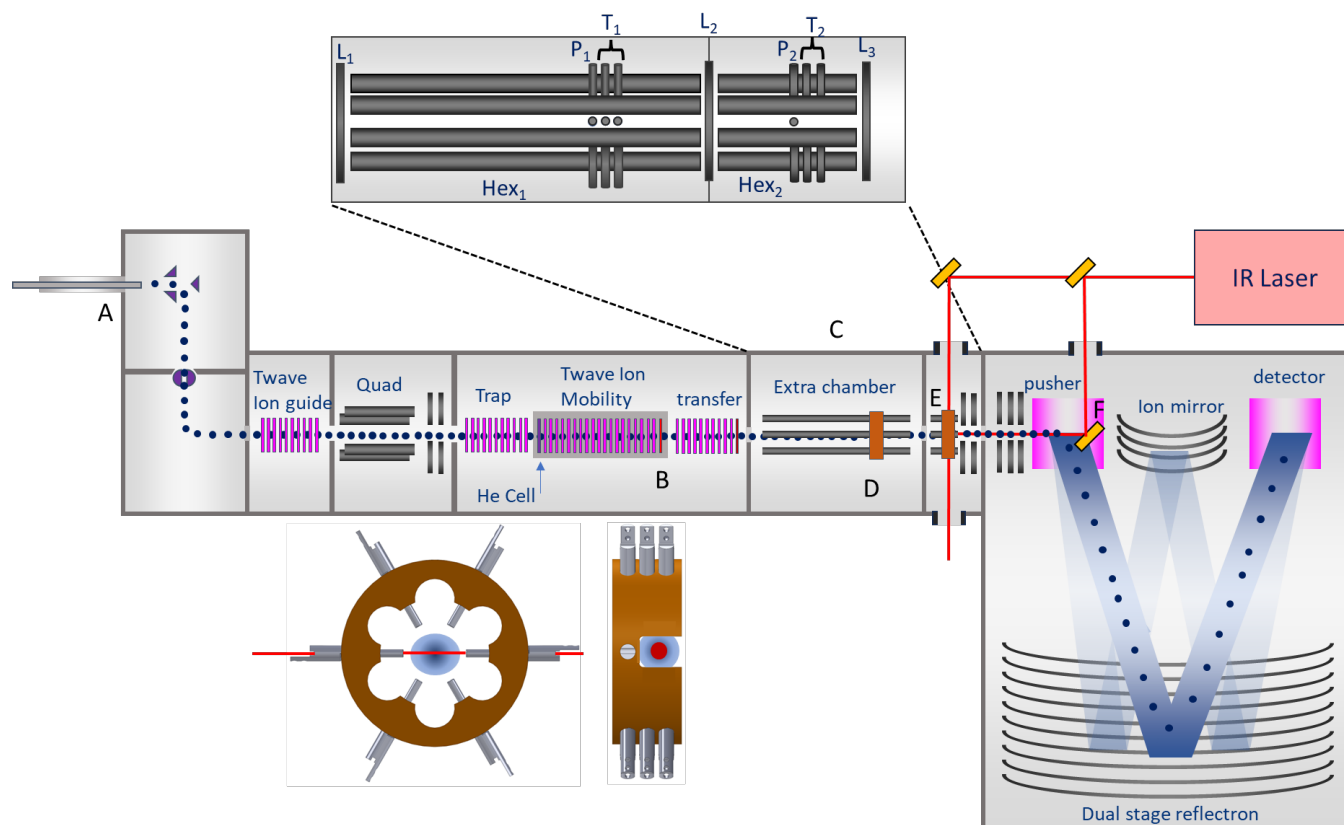


**Figure 1:** A Schematic representation of the Photo-Synapt detailing the modifications indicated by the capital letters. A) Pressure sleeve, B) Ion mobility slicing, C) Additional vacuum chamber. D) First hexapole and pin trap, E) Second hexapole and pin trap, F) Gold mirror for on-axis irradiation. Optical access is also possible perpendicularly to irradiate ions in the second pin trap. An expanded view of the additional ion optics for ion trapping is shown in the top inset, see text and SI for further details. The bottom inset shows a front and side view of the pin traps, indicating the position of the trapped ions and the perpendicular irradiation scheme.

**Vacuum Chamber for Spectroscopy.** Low pressures and long trapping times are essential to perform IR photofragmentation spectroscopy. Therefore, the design of our Photo-Synapt differs from the Synapt G2 modified by the group of Perdita Barran<sup>22, 23</sup>, where irradiation experiments were performed within the trap or transfer TWave. In the Photo-Synapt, the spectrometer was extended with the addition of a vacuum chamber between the transfer TWave and TOF entrance optics (C in Figure 1). This new chamber provides both the required space to perform ion trapping and irradiation, and the differential pumping stage required to achieve a pressure low enough to perform efficient IRMPD (down to  $10^{-6}$  -  $10^{-7}$  mbar).

**Ion Optics Overview.** The top-inset in Figure 1 shows a zoomed illustration of the additional ion optics in the Photo-Synapt for trapping, irradiation, and manipulation of ions. The two hexapoles (Hex<sub>1</sub> and Hex<sub>2</sub>) function as ion guides in transmission mode (i.e. when there is no trapping), with no drop in performance in either MS or IM-MS modes.<sup>20</sup>

In trapping mode, the hexapoles function as ion traps in combination with pulsed lenses L<sub>1</sub> (transfer TWave exit lens), L<sub>2</sub> (new lens), and L<sub>3</sub> (first acceleration electrode). Increasing the voltage on L<sub>2</sub> and L<sub>3</sub> by a few volts relative to the hexapole rods will trap ions within the hexapoles. L<sub>1</sub> is typically operated at a voltage that allows ions from the

source to enter Hex<sub>1</sub>, but its voltage is high enough to prevent ions exiting Hex<sub>1</sub> after collisional cooling. This allows us to continuously fill Hex<sub>1</sub> during measurements resulting in fewer ion losses.

Each hexapole contains a pin trap (see inset at the bottom of Figure 1), which is composed of 3 sets of pins inserted between the hexapole rods of both Hex<sub>1</sub> and Hex<sub>2</sub>. The first set of pins (P<sub>1</sub> and P<sub>2</sub>) are used to transfer ions from the pin traps to Hex<sub>2</sub> or the TOF, respectively.

The second and third sets of pins (T<sub>1</sub> and T<sub>2</sub>) are biased with a small negative voltage relative to the hexapole DC offset. Ions will undergo collisional cooling within the hexapoles, leading them to become trapped in T<sub>1</sub> and T<sub>2</sub>. T<sub>1</sub> is composed of 2 sets of 6 pins, while T<sub>2</sub> is composed of 2 sets of 4 pins. For T<sub>2</sub> a pair of pins have been removed to enable optimal overlap of ion cloud and laser beam.

**Acquisition cycle.** The Photo-Synapt is operated in 3 different states during an acquisition cycle, which we term trapping (and irradiation), ejection, and transfer (see Figure 3 and section S1 of the Supporting Information). Ions undergo a complex sequence of manipulations during this cycle, which can be summarized by the following steps: (i) accumulation of ions into Hex<sub>1</sub> followed by collisional cooling into T<sub>1</sub>, (ii) transfer from T<sub>1</sub> into Hex<sub>2</sub> and subsequent collisional cooling into T<sub>2</sub>, (iii) irradiation in T<sub>2</sub>,

and (iv) ejection to the pusher and detection. To maximize the duty cycle, accumulation of ions in the first trap ( $T_1$ ) and irradiation in the second trap ( $T_2$ ) are performed simultaneously. This results in a shorter acquisition time and fewer wasted ions. These individual steps are discussed in further detail in the Supporting Information (SI.1), and here we summarize what happens to the ions during each instrument state.

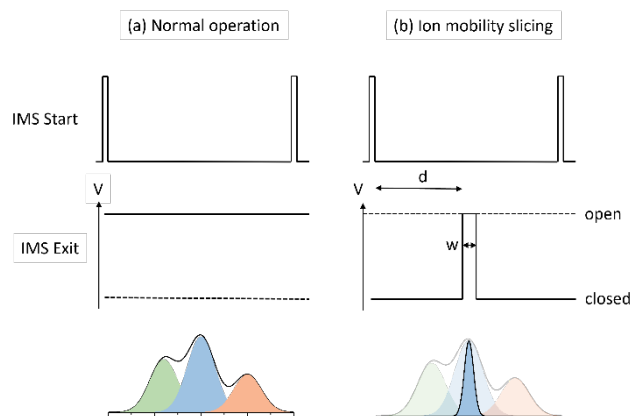


**Figure 2:** Schematic representation of ion mobility slicing in the Photo-Synapt: (a) During normal operation, the IMS exit lens voltage is fixed for maximum transmission, recording the full ion mobility spectrum with three example structures, (b) during ion mobility slicing, the IMS exit lens voltage is kept low to prevent ion transmission and raised after a time  $d$  (relative to the IMS start trigger) for a time  $w$ . This transmits only ions during the time the voltage is high. In the illustrative mobility spectrum, the blue conformation is transmitted while the green and red species are removed.

**Trapping.** In the trapping mode,  $L_2$  is closed and the two hexapoles act as independent traps.  $L_1$  is kept at a voltage that allows ions to enter  $Hex_1$  but prevents them from exiting, leading to constant filling of  $Hex_1$ .  $Hex_1$  is operated at a pressure of between  $10^{-3}$  -  $10^{-5}$  mbar, i.e. ions undergo collisional cooling into  $T_1$ . At the same time, ions that have been transferred to  $Hex_2$  undergo collisional cooling into  $T_2$  and are irradiated with either IR or UV laser pulses.

Ions can be stably trapped in this state for up to 10 seconds, which is only limited by internal MassLynx settings. When using ion mobility slicing, the same conditions are used, with the difference being that the filling of  $Hex_1$  is now linked to the number of ion mobility cycles that occur during the time of the trapping, as ions only reach  $Hex_1$  when the mobility slicing lens is open.

**Ejection.** During the ejection state, ions are ejected from  $T_2$  towards the TOF to be analyzed. This is achieved by simultaneously removing the trapping potential on  $T_2$ , adding a positive potential to  $P_2$ , and setting  $L_3$  to an open state, see Figure 3(b). The TOF pusher is triggered after a set delay, depending on the  $m/z$  of the ions, and subsequently a mass spectrum recorded. As photofragmentation results in ions with a range of  $m/z$  values being present in  $T_2$ , ions will arrive at the pusher at different times (see Supporting Information Figure S2).

Thus, to record all ions, several different pusher delays have to be used within a single acquisition cycle.

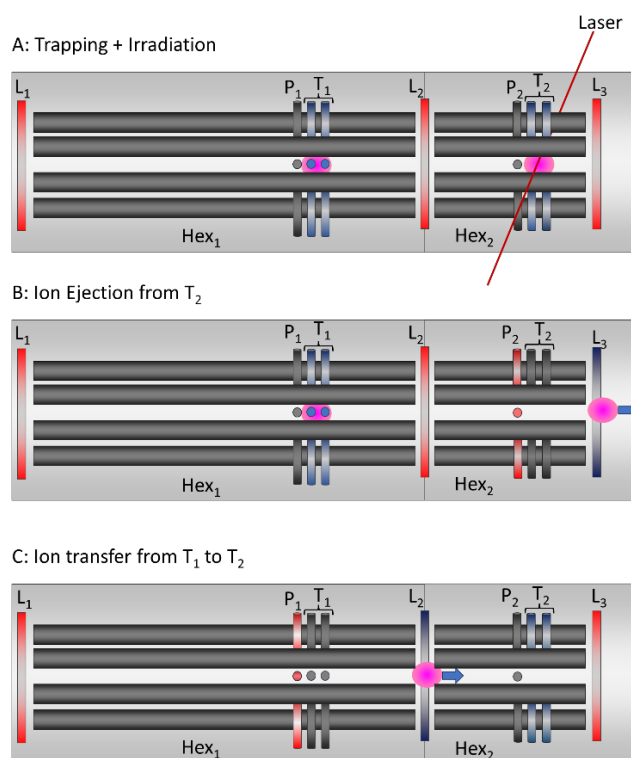


**Figure 3:** Schematic of the different voltage settings used on trapping electrodes during a single cycle showing trapping and irradiation (A), ejection of ions from trap 2 (B) and transfer of ions between trap 1 and trap 2 (C). Typical voltages can be found in Figure S4. A red color indicates a positive voltage (relative to the DC offset of the hexapole), a blue voltage a negative voltage. The pink circle represents the ion cloud.

**Transfer.** During the transfer state, ions are transferred from  $T_1$  towards  $Hex_2$ . To achieve this, a positive pulse is applied to  $P_1$  and  $L_2$  is lowered to allow ions to pass, see Figure 3(c). During this time,  $L_1$  remains open to continue to fill  $Hex_1$ , but ions are blocked from entering  $Hex_2$  by  $P_1$ . As with the situation above, the time it takes ions to reach  $Hex_2$  from  $T_1$  will depend on the  $m/z$ , see Figure S3. However, in this case  $T_1$  typically contains ions of a single  $m/z$ , and thus a single transfer time can be used throughout the acquisition cycle. Once the transfer of ions has been achieved, the electrodes return to the trapping state and this cycle repeats.

## METHODS

**Sample preparation VEALYL.** Aliquots of the hexapeptide VEALYL, a peptide segment from the B chain of insulin (purity >95%, GeneCust) were dissolved in 50:50 v/v water:methanol at a concentration of 200  $\mu$ M.<sup>9</sup> These samples were prepared on the day of measurement, loaded in gold-coated nano-electrospray emitters and introduced into the Photo-Synapt using nano-ESI in positive ion mode. Source and IM-MS parameters that were used: capillary voltage at 0.35 kV, sampling cone at 45V for the 2<sup>+</sup> and 15V

for the  $4^{2+}$  and the  $6^{3+}$ , desolvation temperature of 150 °C, source temperature of 80 °C, trap gas flow 2 mL/min, helium gas flow 180 mL/min, IMS gas flow 40 mL/min, IMS wave velocity 400 m/s and the IMS wave height at 20V.

**Sample preparation glycan fragments.** Human alpha-1-acid glycoprotein (hAGP) stock solution (1 mg/mL in 100 mM ammonium acetate buffer), was diluted to 50 µg/mL in water:acetonitrile:formic acid (1:1:0.05 v/v/v%). Transferrin (TF) was diluted to 100 µg/mL in water:acetonitrile:formic acid (1:1:0.05 v/v/v%). Both hAGP and TF were directly infused using electrospray ionization (120 µL/hr) in positive ion mode. For ion mobility separation an IMS gas flow of 90 mL/min was used, a wave velocity of 650 m/s and a wave height of 40 V.<sup>35</sup>

**Laser** – A tunable infrared laser (FireFly IR, M-Squared) was used for the reported IR spectroscopic experiments. The laser is tunable between 2700 – 4000  $\text{cm}^{-1}$ , has an output power of more than 80 mW, pulse durations of <10 ns, and was operated at a 150 kHz repetition rate.

**Data processing** – MassLynx V4.1 (MassLynx software instrument control) was used to obtain the mass and mobility data; Origin 2023 was used to analyze and plot the data.

## RESULTS AND DISCUSSION

**IR action spectroscopy of mass- and mobility-selected VEALYL oligomers.** The peptide VEALYL, a segment from the B chain of insulin, was selected to illustrate the capabilities of the Photo-Synapt to create IR spectra of mass- and mobility selected oligomers. This six-residue sequence has a high propensity to form amyloid aggregates and therefore has been the topic of many studies.<sup>14, 36, 37</sup>

Figure 4a shows the mass spectrum of freshly prepared VEALYL (full MS can be found in Figure S5). The dominant peak at  $m/z$  707 in the mass spectrum originates from the singly charged monomer ( $1^{1+}$ ), or more precisely from  $[n]^{n+}$  type oligomers with  $n$  the number of monomeric units. Furthermore, the doubly charged monomer adducted with potassium ( $[1+H+K]^{2+}$ ) is present at  $m/z$  373 and a small peak is observed around  $m/z$  1413, which could correspond to  $[2n]^{n+}$  oligomers, such as the  $2^{1+}$ ,  $4^{2+}$ , and  $6^{3+}$  species. Figure 4b displays a zoomed-in portion of the  $m/z$  1413 quadrupole filtered mass spectrum, indicating the presence of more isobaric species present than just the  $2^{1+}$  dimer. Subsequently, we have employed ion mobility on the quadrupole selected oligomers, which allows the separation and identification of individual oligomers with the same  $m/z$  ratio, see Figure 4c. To assign the mobility peaks, the isotopic distribution of the extracted mass spectra of each mobility peak is evaluated, see Figure 4d-f.

The most intense peak in Figure 4c (red) originates from the mobility of the dimer singly charged ( $2^{1+}$ ), the consecutive two other intense peaks (highlighted in green and blue resp.) result from the doubly charged tetramer  $4^{2+}$  and the triply charged hexamer  $6^{3+}$ , followed by a small peak originating from the  $8^{4+}$  oligomer. Even though the quadrupole mass filter was used to only select  $[2n]^{n+}$  oligomers with  $m/z$  1413, several other signatures

appeared in the mobility spectrum, such as the  $1^{1+}$  and in lower abundances  $3^{2+}$ ,  $5^{2+}$ ,  $7^{3+}$  and  $9^{4+}$  oligomers. These oligomer-fragments result from fragmentation of the quadrupole selected  $[2n]^{n+}$  oligomers after the mass filter and before the ion mobility separation (i.e. in the trap cell). Here, our main goal was to get high transmission of the oligomers, therefore all parameters were set for optimal transmission, at the cost of some fragmentation in the trap cell. By using the ion mobility slicing these unwanted fragments are removed.

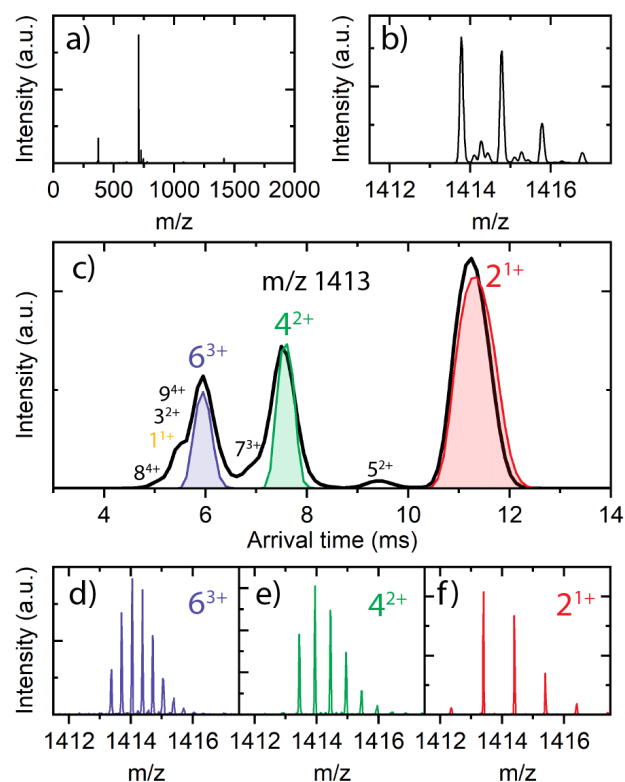


**Figure 4.** a) Full mass spectrum of freshly prepared VEALYL; b) zoomed-in mass spectrum of quadrupole mass filtered  $m/z$  1413; c) arrival time distribution of quadrupole selected  $m/z$  1413 of VEALYL, the detected oligomers are annotated; d), e) and f) the obtained mass spectrum after slicing and trapping of the  $6^{3+}$ ,  $4^{2+}$ , and  $2^{1+}$ , respectively.

With quadrupole and ion mobility selection combined, only the oligomer ions with specific  $m/z$  and selected mobility are transferred into the traps ( $T_1$  and  $T_2$ ), as indicated by the colored traces in Figure 4c. Consequently, the mass spectra presented in Figure 4d-f result *only* from species that are stored in the traps, as other ions are selectively filtered out by either the quadrupole mass filter or the mobility slicing. Subsequently, the selected and trapped oligomer ions are irradiated for about 400 to 1000 ms in trap  $T_2$ . The resulting photofragments are transferred and analyzed at the TOF. By repeating this experiment over the entire IR wavelength of interest, their IR action spectrum can be recorded. To plot such an IR action spectrum, the photofragmentation per wavelength is calculated using:

$$\text{Photofragmentation yield} = -\ln\left(\frac{I_{\text{prec}}}{\sum I_{\text{frag}} + I_{\text{prec}}}\right) \quad (1)$$

with  $\sum I_{frag}$  the sum of the intensity of all the primary fragments and  $I_{prec}$  the intensity of the precursor ion. This method of calculating the photofragmentation yield makes it possible to linearly correct for the irradiation time and the laser power.<sup>38, 39</sup> IR multiphoton dissociation (IRMPD) results in general in similar fragmentation pathways as collision induced dissociation (CID), where the weakest bond is broken, see Supporting Information Figure S6a-b. Determining the IR photofragmentation yield, and thus plotting the IR spectrum, can be quite challenging when studying an aggregation process. Formed oligomer-photofragments of larger oligomers are stable in the trap and can absorb the IR radiation as well. This would result in an overlapping IR signature of the mass- and mobility-selected oligomer and the formed oligomer-photofragments, which often are lower-order oligomers that we just carefully removed. Therefore, it is essential to take only primary photofragments into account when determining the photofragmentation yield.

For the  $2^{1+}$  oligomer, both CID and IRMPD at  $2970\text{ cm}^{-1}$  show that this oligomer fragments exclusively into the  $1^{1+}$  m/z channel. Therefore, we can use the intact singly charged monomer ( $1^{1+}$ ) as the primary fragment to calculate the photofragmentation yield (1). The  $4^{2+}$  species could theoretically fragment into a trimer, dimer, and/or monomer, however, CID (Figure S6c) shows that the  $4^{2+}$  oligomer exclusively fragments into the  $2^{1+}$  species, which is confirmed by the IRMPD data presented in Figure S6d. Of course, the photofragmentation routes can become more complex for the higher-order oligomers, which is clearly illustrated by the  $6^{3+}$  oligomer (see Figure S6e-f). The CID spectrum shows the simultaneous fragmentation of the  $6^{3+}$  oligomer into  $5^{2+}$ ,  $4^{2+}$  and  $2^{1+}$  m/z channels, while the IR data suggests that  $4^{2+}$  photofragment is formed before the  $2^{1+}$  photofragment. To determine the photofragmentation yield, we have used the  $5^{2+}$  and the  $4^{2+}$  as the primary fragments for  $6^{3+}$ , as we cannot exclude the possibility that the  $2^{1+}$  is a secondary fragment of the  $4^{2+}$  oligomer. The individual intensities of the precursor ion, which have overlapping m/z values for our oligomer series ( $2^{1+}$ ,  $4^{2+}$  and  $6^{3+}$ ), are derived from their expected isotopic ratios (see Supporting Information Section S2, Figures S7, S8 and Table S1 for details). Although an approximation, it reflects the reality more accurately than when the full m/z = 1413 range was taken as precursor (as the formed photofragments can also appear in this m/z channel).

The mass- and mobility-selective IR photofragmentation spectra of the  $2^{1+}$ ,  $4^{2+}$  and  $6^{3+}$  oligomers are measured in the X-H stretching region (with X = C, N or O) from  $2700$  to  $3700\text{ cm}^{-1}$  (Figure 5b-d) and plotted together with the singly charged monomer ( $1^{1+}$ ) for comparison (Figure 5a). The spectra are all averaged over >5 individual scans and subsequently smoothed (raw data is presented in Figure S9 together with the singly charged monomer). Scans with different irradiation times were linearly corrected to match each other. The spectra of  $2^{1+}$ ,  $4^{2+}$  and  $6^{3+}$  are built up in a similar way: a weak OH stretch vibration at  $3646\text{ cm}^{-1}$  (not observed for  $6^{3+}$ ), indicating a free OH stretch vibration, originating from the Tyr-OH<sup>40</sup>; a broad feature between

$3250$  and  $3400\text{ cm}^{-1}$ , which can be attributed to hydrogen bonded N-H stretching vibrations; a strong and sharp feature at  $2970\text{ cm}^{-1}$ , and a smaller and broader peak at  $2940\text{ cm}^{-1}$ , both likely C-H stretch vibrations. Additionally, there is activity between  $3000$  and  $3300\text{ cm}^{-1}$  in the form of a broad and featureless elevated yield.

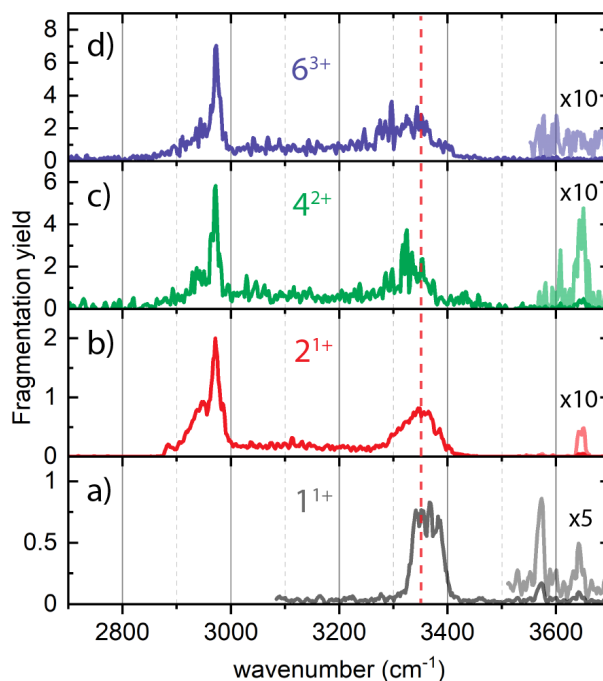


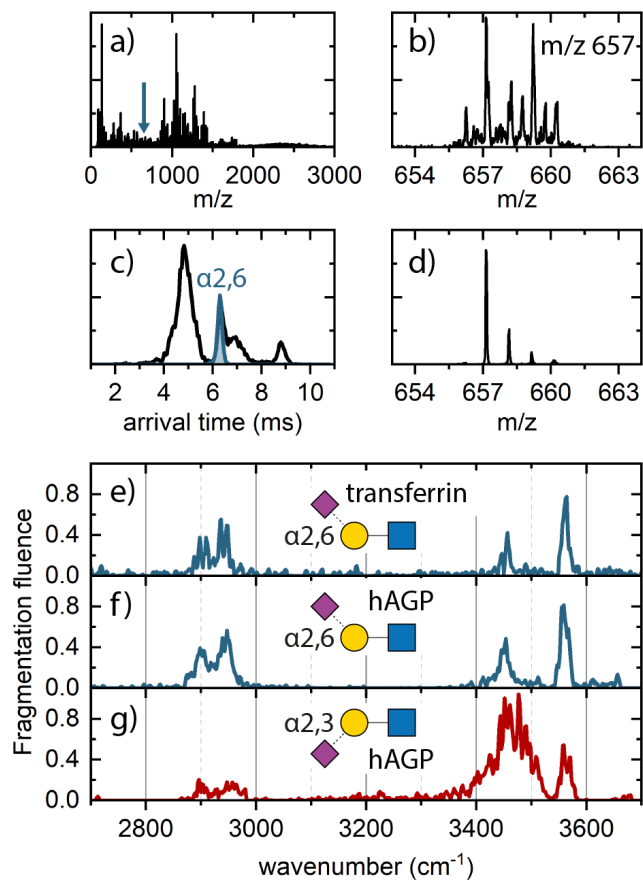
**Figure 5.** IR photofragmentation spectra of the a)  $1^{1+}$  (grey), b)  $2^{1+}$  (red), c)  $4^{2+}$  (green) and d)  $6^{3+}$  (blue) between  $2700$  and  $3700\text{ cm}^{-1}$ . The red dashed line shows the peak position of the  $2^{1+}$  and highlights the redshift in the spectra of the  $4^{2+}$  and  $6^{3+}$ .

Although the IR spectra look at first glance quite similar, the spectra differ clearly in the N-H stretch region. In Figure 5b, the  $2^{1+}$  shows a broad peak between  $3300$  and  $3400\text{ cm}^{-1}$  with its maximum around  $3350\text{ cm}^{-1}$  (indicated with the red dashed line), redshifted by  $15\text{ cm}^{-1}$  with respect to the  $1^{1+}$  (Figure 5a). With increasing aggregations, this NH band continues to broaden and shift to lower wavenumbers (Figure 5c-d), with the  $6^{3+}$  showing strong features down to  $3250\text{ cm}^{-1}$ . The  $1^{1+}$  spectrum shows an additional peak at  $3573\text{ cm}^{-1}$ , which is not present in the other spectra. This indicates that the c-terminal -OH and/or the glutamic acid -OH is/are likely involved in hydrogen bonding upon aggregation. The combination of both mass and mobility selection makes it possible to obtain infrared spectra of isobaric oligomers, which allows for more detailed experimental research into oligomerization and fragmentation pathways of peptides.

**IR signatures of isomers of glycan fragments.** Proteins can exhibit intricate glycan structures that shape their physical properties, half-life and receptor recognition.<sup>41</sup> Understanding these interactions requires knowledge of the exact glycan structure, as different isomeric features can lead to different biological activities. Sialic acid linkages play a crucial role as many glycan structures are terminated with sialic acid, making it an easily accessible glycan epitope

for biomolecular interactions. The most common sialic acid linkages are the  $\alpha 2,3$  and  $\alpha 2,6$  isomers which are relevant in human virus entry or cancer biology.<sup>42-44</sup> Despite their biological significance, the analysis of these isomers presents an analytical challenge. Recent studies have shown that IR-MS enables direct identification of sialic acid linkage.<sup>27, 45-49</sup> The fragmentation of sialylated glycans yield characteristic oxonium ions, such as the sialyllactose trisaccharide at  $m/z$  657 which exhibits distinct ion mobility features depending on sialic acid linkage.<sup>50, 51</sup>

**Figure 6.** a) Full mass spectrum of transferrin under harsh



source conditions, blue arrow indicates the location of the  $m/z$  657 fragment, b) Quadrupole filtered mass spectrum of  $m/z$  657, c) Full arrival time distribution (black) for the mass filtered  $m/z$  657, blue indicates the sliced section corresponding to the  $\alpha 2,6$  isomer of TF, d) Mass spectrum of the mass filtered, and ion mobility sliced  $m/z$  657 fragment. Quadrupole selected ( $m/z$  657), and IM sliced IR spectra of e) transferrin  $\alpha 2,6$ -linked sialic acid isomer, b) human- $\alpha$ -glycoprotein  $\alpha 2,6$ , and c) human- $\alpha$ -glycoprotein  $\alpha 2,3$  isomer.

We use this sialylated N-glycan fragment ( $m/z$  657) to demonstrate the possibility of the Photo-Synapt to obtain mass and ion mobility selected infrared spectra from mixtures of  $\alpha 2,6$ - and  $\alpha 2,3$ -linked sialic acid isomers that are directly extracted from glycoproteins. Therefore, the full glycoproteins, i.e. transferrin and hAGP, were dissolved and introduced in the mass spectrometer using nano-ESI in positive mode. Employing harsh source conditions (2.1-2.3 kV capillary voltage, 90-130 V sampling cone), the

glycoprotein significantly fragmented, resulting in the  $m/z$  657 B3 fragments amongst other, see Figure 6a.

Since transferrin (TF) predominantly holds the  $\alpha 2,6$  sialylated fragment ( $\alpha 2,6:\alpha 2,3 = 95:5$ ), TF will provide a clear IM and IR signature for the  $\alpha 2,6$  isomer. Figure 6a-d shows the workflow for generating, mass selecting, and mobility slicing the  $\alpha 2,6$  isomer of TF. Using the quadrupole mass filter, the sialylated  $m/z$  657 fragment was isolated, indicated by the arrow in the full mass spectrum in Figure 6a, resulting in the mass spectrum presented in Figure 6b. The signature is a combination of residual fragments of the TF protein combined with the sialylated N-glycan fragment. The ion mobility spectrum was recorded of the quadrupole selected  $m/z$  657 region was recorded (see Figure S10a), and the mobility peak corresponding to the  $\alpha 2,6$  isomer was identified by analyzing the mobility extracted mass spectra, see Supporting Information Figure S10c-f. Subsequently, ion mobility slicing was used to isolate the  $\alpha 2,6$  isomer (Figure 6c, highlighted in blue), resulting in a clean mass and ion mobility selected mass spectrum of the  $m/z$  657 fragment. Finally, the mass and mobility selected IR spectrum of the B3 fragment originating from the TF glycoprotein was recorded, see Figure 6e.

The same process was used for human  $\alpha 1$ -acid-glycoprotein (hAGP), which is shown in detail in Figure S11 of the Supporting Information. In contrast to TF, both  $\alpha 2,6:\alpha 2,3$ -isomers are present in hAGP, with the ratio depending on the antenna type.<sup>35, 50</sup> Here, for the direct fragments from the full hAGP protein, we observe a 78:22 ratio for  $\alpha 2,6:\alpha 2,3$  isomeric ratio, indicated in by the label V and VI in Figure S11c. We have recorded the mass and mobility selected IR spectra of the B3 fragments originating from both the  $\alpha 2,6$  isomer (Figure 6f, blue trace) and the  $\alpha 2,3$  isomer (Figure 6g, red trace) from hAGP.

To record the infrared spectra of the  $m/z$  657 B3 fragment ions, we trapped and irradiated the ions for 2 seconds, after which we detected the precursor mass and the fragment mass ( $m/z$  366) using two different time delays. The photofragmentation yield is calculated via equation (1) and the resulting spectra are plotted in Figure 6e-g. The raw data is presented in Figure S12. The  $\alpha 2,6$  isomer of hAGP shows an identical IR spectrum as TF (Figure 6e) which confirms that both species are the  $\alpha 2,6$  isomer. The  $\alpha 2,3$  isomer, with a slightly later ion mobility arrival time, clearly shows a dissimilar IR spectrum compared to the  $\alpha 2,6$  isomer. Even though, the peak position at  $3560 \text{ cm}^{-1}$  is similar for both isomers, the region between  $3400$  and  $3530 \text{ cm}^{-1}$  is visibly different (all attributed to OH stretch vibrations). Where the  $\alpha 2,6$  isomer shows a single intense peak at  $3450 \text{ cm}^{-1}$  and some minor activity around  $3500 \text{ cm}^{-1}$ , the spectrum of the  $\alpha 2,3$  isomer shows a broad band covering a wide region. Additionally, the ratio in peak intensity between  $3560$  and  $3450 \text{ cm}^{-1}$  is reversed, with the  $\alpha 2,3$  isomer showing more intensity in the lower wavelength region. The CH pattern observed below  $3000 \text{ cm}^{-1}$  is quite similar for both isomers with two main features present at  $2900$  and  $2942 \text{ cm}^{-1}$ . Although, we have measured the sialyllactose trisaccharide cleaved from full glycoproteins compared to the isolated 3'- and 6'-sialyl-N-

acetyllactosamine by Depraz Depland et al.<sup>47</sup>, a similar trend is observed in the IR spectra; the  $\alpha$ 2,3 isomer shows a very broad spectrum in the OH range, while  $\alpha$ 2,6 isomer results in resolved spectra.

The combination of both m/z selection and ion mobility slicing results in recording unique IR spectra of allows us to record and identify sialylated N-glycan fragments from glycoproteins without any pre-separation technique via their unique infrared spectra.

## CONCLUSIONS

In this paper, we have demonstrated the strength of combining ion mobility, mass spectrometry and IR action spectroscopy in one single experiment. Therefore, we have developed and applied a three-dimensional hyphenated mass spectrometer: the Photo-Synapt. This combination makes it possible to select a specific analyte with mass spectrometry, subsequently to separate a conformational structure with ion mobility and record the specific vibrational signatures of the mass and mobility selected species by IR action spectroscopy.

The Photo-Synapt, is initially developed to Probe Higher Order Transient Oligomers; important species along the aggregation pathway of peptides and proteins related to neurodegenerative diseases. Employing the Photo-Synapt, we have followed the oligomer formation in the  $[n]^{2nz+}$  m/z channel. By selecting this oligomer type with a quadrupole mass filter, then separating and identifying the present oligomers ranging from singly charged dimers to quadruply charged octamers within this m/z channel using ion mobility, and employing mobility slicing to isolate a specific isomer, we have been able to observe unique IR features in the NH stretching vibrational region for each oligomer. Furthermore, combining m/z selection with ion mobility slicing enables the direct identification of the linkage of sialylated N-glycan fragments from glycoproteins through their distinctive infrared spectra, eliminating the need for pre-separation techniques.

## ASSOCIATED CONTENT

### Data Availability Statement

The data underlying this study are openly available in DataCite Commons at [upon publication]

### Supporting Information

The Supporting Information is available free of charge on the ACS Publications website. Supporting information: Additional experimental details, raw data and detailed clarifying explanations on the instrumentation and data acquisition. (PDF)

## AUTHOR INFORMATION

### Corresponding Author

\* **Anouk M. Rijs** – Division of Bioanalytical Chemistry, Vrije Universiteit Amsterdam, 1081 HV Amsterdam, the Netherlands; orcid.org/0000-0002-7446-9907; Email: a.m.rijs@vu.nl

### Author Contributions

The manuscript was written through contributions of all authors. All authors have given approval to the final version of the manuscript. S.B., S.D.: experimental, methodology, conceptualization, writing original draft. B.D.: instrumental support, review. M.B.: experimental, review. J.C.: methodology, review. A.M.R.: experimental, methodology, supervision, conceptualization, funding acquisition, and writing.

## ACKNOWLEDGMENT

The authors gratefully acknowledge funding from the research program VICI with project number VI.C.192.024 and Aspasia (015.015.009) from the Dutch Research Council (NWO) awarded to A.M.R. We would like to thank all members from the MS-Laserlab (Vrije Universiteit Amsterdam), and especially Iuliia Stroganova, Agatahe Depraz Depland and Kevin Hes, for helpful discussions.

## REFERENCES

- (1) Ashcroft, A. E. *J. Am. Soc. Mass. Spectrom.* **2010**, *21* (7), 1087-1096.
- (2) Laganowsky, A.; Liu, C.; Sawaya, M. R.; Whitelegge, J. P.; Park, J.; Zhao, M. L.; Pensalfini, A.; Soriaga, A. B.; Landau, M.; Teng, P. K.; Cascio, D.; Glabe, C.; Eisenberg, D. *Science* **2012**, *335* (6073), 1228-1231.
- (3) Neudecker, P.; Robustelli, P.; Cavalli, A.; Walsh, P.; Lundstrom, P.; Zarrine-Afsar, A.; Sharpe, S.; Vendruscolo, M.; Kay, L. E. *Science* **2012**, *336* (6079), 362-366.
- (4) Knowles, T. P.; Vendruscolo, M.; Dobson, C. M. *Nat. Rev. Mol. Cell Biol.* **2014**, *15* (6), 384-396.
- (5) Arosio, P.; Knowles, T. P.; Linse, S. *Phys. Chem. Chem. Phys.* **2015**, *17* (12), 7606-7618.
- (6) Tanaka, M.; Komi, Y. *Nat. Chem. Biol.* **2015**, *11* (6), 373-377.
- (7) Pukala, Tara L. *Essays Biochem.* **2023**, *67* (2), 243-253.
- (8) *Ion Mobility – Mass Spectrometry: Fundamentals and Applications*; The Royal Society of Chemistry, 2021. DOI: 10.1039/9781839162886.
- (9) Bleiholder, C.; Dupuis, N. F.; Wyttenbach, T.; Bowers, M. T. *Nat. Chem.* **2011**, *3* (2), 172-177.
- (10) Woods, L. A.; Radford, S. E.; Ashcroft, A. E. *Biochim. Biophys. Acta Proteins Proteom.* **2013**, *1834* (6), 1257-1268.
- (11) Liu, Y.; Graetz, M.; Ho, L.; Pukala, T. L. *Eur. J. Mass Spectrom.* **2015**, *21* (3), 255-264.
- (12) Phillips, A. S.; Gomes, A. F.; Kalapothakis, J. M. D.; Gillam, J. E.; Gasparavicius, J.; Gozzo, F. C.; Kunath, T.; MacPhee, C.; Barran, P. E. *Analyst* **2015**, *140* (9), 3070-3081.
- (13) Young, L. M.; Saunders, J. C.; Mahood, R. A.; Revill, C. H.; Foster, R. J.; Ashcroft, A. E.; Radford, S. E. *Methods* **2016**, *95*, 62-69.
- (14) Seo, J.; Hoffmann, W.; Warnke, S.; Huang, X.; Gewinner, S.; Schöllkopf, W.; Bowers, M. T.; von Helden, G.; Pagel, K. *Nat. Chem.* **2017**, *9* (1), 39-44.
- (15) Young, L. M.; Ashcroft, A. E.; Radford, S. E. *Curr. Opin. Chem. Biol.* **2017**, *39*, 90-99.
- (16) Laos, V.; Do, T. D.; Bishop, D.; Jin, Y.; Marsh, N. M.; Quon, B.; Fetters, M.; Cantrell, K. L.; Buratto, S. K.; Bowers, M. T. *ACS Chem. Neurosci.* **2019**, *10* (9), 4112-4123.
- (17) Moons, R.; van der Wekken-de Bruijne, R.; Maudsley, S.; Lemièrre, F.; Lambeir, A.-M.; Sobott, F. *Int. J. Mol. Sci.* **2020**, *21* (21), 7884.
- (18) Liu, X.; Ganguly, P.; Jin, Y.; Jhatro, M. J.; Shea, J.-E.; Buratto, S. K.; Bowers, M. T. *J. Am. Chem. Soc.* **2022**, *144* (32), 14614-14626.
- (19) Depraz Depland, A.; Stroganova, I.; Wootton, C. A.; Rijs, A. M. *J. Am. Soc. Mass. Spectrom.* **2023**, *34* (2), 193-204.
- (20) Stroganova, I.; Willenberg, H.; Tente, T.; Depraz Depland, A.; Bakels, S.; Rijs, A. M. *Anal. Chem.* **2024**, *96*, 5115-5124.



- (21) Hoffmann, W.; Folmert, K.; Moschner, J.; Huang, X.; von Berlepsch, H.; Kokscho, B.; Bowers, M. T.; von Helden, G.; Pagel, K. *J. Am. Chem. Soc.* **2018**, *140* (1), 244-249.
- (22) Bellina, B.; Brown, J. M.; Ujma, J.; Murray, P.; Giles, K.; Morris, M.; Compagnon, I.; Barran, P. E. *Analyst* **2014**, *139* (24), 6348-6351.
- (23) Theisen, A.; Yan, B.; Brown, J. M.; Morris, M.; Bellina, B.; Barran, P. E. *Anal. Chem.* **2016**, *88* (20), 9964-9971.
- (24) Miller, S. A.; Jeanne Dit Fouque, K.; Ridgeway, M. E.; Park, M. A.; Fernandez-Lima, F. *J. Am. Soc. Mass. Spectrom.* **2022**, *33* (7), 1267-1275.
- (25) Liu, F. C.; Ridgeway, M. E.; Wootton, C. A.; Theisen, A.; Panczyk, E. M.; Meier, F.; Park, M. A.; Bleiholder, C. *J. Am. Soc. Mass. Spectrom.* **2023**, *34* (10), 2232-2246.
- (26) Stroganova, I.; Rijs, A. M. Ion Spectroscopy Coupled to Ion Mobility–Mass Spectrometry. In *Ion Mobility – Mass Spectrometry: Fundamentals and Applications*, Ashcroft, A. E., Sobott, F. Eds.; The Royal Society of Chemistry, 2021; pp 206-242.
- (27) Grabarics, M.; Lettow, M.; Kirschbaum, C.; Greis, K.; Manz, C.; Pagel, K. *Chem. Rev.* **2022**, *122* (8), 7840-7908.
- (28) Yatsyna, V.; Abikhodr, A. H.; Ben Faleh, A.; Warnke, S.; Rizzo, T. R. *Anal. Chem.* **2022**, *94* (6), 2912-2917.
- (29) Wang, Y.; Alhajji, E.; Rieul, B.; Berthias, F.; Maitre, P. *Int. J. Mass Spectrom.* **2019**, *443*, 16-21.
- (30) Schindler, B.; Depraz Depland, A.; Renois-Predelus, G.; Karras, G.; Concina, B.; Celep, G.; Maurelli, J.; Lorient, V.; Constant, E.; Bredy, R.; Bordas, C.; Lépine, F.; Compagnon, I. *Int. J. Ion Mobil. Spectrom.* **2017**, *20* (3), 119-124.
- (31) Giuliani, A.; Williams, J. P.; Green, M. R. *Anal. Chem.* **2018**, *90* (12), 7176-7180.
- (32) Simke, F.; Fischer, P.; Damjanović, T.; Kádek, A.; Kierspel, T.; Lorenzen, K.; Uetrecht, C.; Schweikhard, L. *J. Instrum.* **2023**, *18* (10), P10021.
- (33) Simke, F.; Fischer, P.; Marx, G.; Schweikhard, L. *Int. J. Mass Spectrom.* **2022**, *473*, 116779.
- (34) van den Heuvel, R. H.; van Duijn, E.; Mazon, H.; Synowsky, S. A.; Lorenzen, K.; Versluis, C.; Brouns, S. J.; Langridge, D.; van der Oost, J.; Hoyes, J. *Anal. Chem.* **2006**, *78* (21), 7473-7483.
- (35) Guttman, M.; Lee, K. K. *Anal. Chem.* **2016**, *88* (10), 5212-5217.
- (36) Ivanova, M. I.; Thompson, M. J.; Eisenberg, D. *Proc. Natl. Acad. Sci. U.S.A.* **2006**, *103* (11), 4079-4082.
- (37) Roeters, S. J.; Sawall, M.; Eskildsen, C. E.; Panman, M. R.; Tordai, G.; Koeman, M.; Neymeyr, K.; Jansen, J.; Smilde, A. K.; Woutersen, S. *Biophys. J.* **2020**, *119* (1), 87-98.
- (38) Berden, G.; Derksen, M.; Houthuijs, K. J.; Martens, J.; Oomens, J. *Int. J. Mass Spectrom.* **2019**, *443*, 1-8.
- (39) Moge, B.; Yeni, O.; Infantino, A.; Compagnon, I. *Int. J. Mass Spectrom.* **2023**, *490*, 117071.
- (40) Sinha, R. K.; Chiavarino, B.; Crestoni, M. E.; Scuderi, D.; Fornarini, S. *Int. J. Mass Spectrom.* **2011**, *308* (2-3), 209-216.
- (41) Varki, A. *Glycobiol.* **2017**, *27* (1), 3-49.
- (42) Dobie, C.; Skropeta, D. *Br. J. Cancer* **2021**, *124* (1), 76-90.
- (43) Wielgat, P.; Rogowski, K.; Godlewska, K.; Car, H. *Cells* **2020**, *9* (9), 1963.
- (44) Pearce, O. M.; Läubli, H. *Glycobiol.* **2016**, *26* (2), 111-128.
- (45) Gray, C. J.; Schindler, B.; Migas, L. G.; Pičmanová, M.; Allouche, A. R.; Green, A. P.; Mandal, S.; Motawia, M. S.; Sánchez-Pérez, R.; Bjarnholt, N.; Møller, B. L.; Rijs, A. M.; Barran, P. E.; Compagnon, I.; Evers, C. E.; Flitsch, S. L. *Anal. Chem.* **2017**, *89* (8), 4540-4549.
- (46) Schindler, B.; Barnes, L.; Renois, G.; Gray, C.; Chambert, S.; Fort, S.; Flitsch, S.; Loison, C.; Allouche, A.-R.; Compagnon, I. *Nat. Comm.* **2017**, *8* (1), 973.
- (47) Depraz Depland, A.; Renois-Predelus, G.; Schindler, B.; Compagnon, I. *Int. J. Mass Spectrom.* **2018**, *434*, 65-69.
- (48) Elferink, H.; Severijnen, M. E.; Martens, J.; Mensink, R. A.; Berden, G.; Oomens, J.; Rutjes, F. P.; Rijs, A. M.; Boltje, T. J. *J. Am. Chem. Soc.* **2018**, *140* (19), 6034-6038.
- (49) Ben Faleh, A.; Warnke, S.; Bansal, P.; Pellegrinelli, R. P.; Dyukova, I.; Rizzo, T. R. *Anal. Chem.* **2022**, *94* (28), 10101-10108.
- (50) Manz, C.; Mancera-Arteu, M.; Zappe, A.; Hanozin, E.; Polewski, L.; Giménez, E.; Sanz-Nebot, V.; Pagel, K. *Anal. Chem.* **2022**, *94* (39), 13323-13331.
- (51) Hinneburg, H.; Hofmann, J.; Struwe, W. B.; Thader, A.; Altmann, F.; Silva, D. V.; Seeberger, P. H.; Pagel, K.; Kolarich, D. *Chem. Commun.* **2016**, *52* (23), 4381-4384.

For table of contents only

